Robust superconductivity and the suppression of charge-density wave in the quasi-skutterudites $Ca_3(Ir_{1-x}Rh_x)_4Sn_{13}$ single crystals at ambient pressure

Elizabeth H. Krenkel,[1,2] Makariy A. Tanatar,[1,2] Sunil Ghimire,[1,2] Kamal R. Joshi,[1] Shuzhang Chen,[3,4] Cedomir Petrovic,[3,4] and Ruslan Prozorov[1,2,*]

[1] *Ames National Laboratory, Ames, Iowa 50011, USA*
[2] *Department of Physics & Astronomy, Iowa State University, Ames, Iowa 50011, USA*
[3] *Condensed Matter Physics and Materials Science Department, Brookhaven National Laboratory, Upton, New York 11973, USA*
[4] *Department of Physics and Astronomy, Stony Brook University, Stony Brook, New York 11794-3800, USA*

(Dated: 4 April 2024)

Single crystals of the quasi-skutterudite compounds $Ca_3(Ir_{1-x}Rh_x)_4Sn_{13}$ (3-4-13) were synthesized by flux growth and characterized by X-ray diffraction, energy dispersive X-ray spectroscopy, magnetization, resistivity, and radio frequency magnetic susceptibility techniques. The coexistence and competition between the charge density wave (CDW) and superconductivity was studied by varying the Rh/Ir ratio. The superconducting transition temperature, T_c, varies from 7 K in pure Ir ($x = 0$) to 8.3 K in pure Rh ($x = 1$). Temperature-dependent electrical resistivity reveals monotonic suppression of the CDW transition temperature, $T_{CDW}(x)$. The CDW starts in pure Ir, $x = 0$, at $T_{CDW} \approx 40$ K and extrapolates roughly linearly to zero at $x_c \approx 0.53 - 0.58$ under the superconducting dome. Magnetization and transport measurements show a significant influence of CDW on superconducting and normal states. Meissner expulsion is substantially reduced in the CDW region, indicating competition between the CDW and superconductivity. The low-temperature resistivity is higher in the CDW part of the phase diagram, consistent with the reduced density of states due to CDW gapping. Its temperature dependence just above T_c shows signs of non-Fermi liquid behavior in a cone-like composition pattern. We conclude that the $Ca_3(Ir_{1-x}Rh_x)_4Sn_{13}$ alloy is a good candidate for a composition-driven quantum critical point (QCP) at ambient pressure.

I. INTRODUCTION

The family of materials with the general formula $R_3T_4X_{13}$ was discovered in 1980 and is frequently referred to as Remeika 3-4-13 compounds [1]. Here, R stands for alkali, rare earth, or actinide metals, T stands for a transition metal and X can be Sn, Ge, or In. In this large family of materials (more than 1200 compounds, see Ref.2 for a review), cage-like structures and strong electronic correlations provide the possibility to alter both the electronic and lattice degrees of freedom and result in many interesting properties. These materials are studied as potential thermoelectrics [3–5]. Heavy fermion behavior is found in compounds such as $Ce_3Co_4Sn_{13}$ [6], $Pr_3Os_4Ge_{13}$ [7], $Ce_3Rh_4Sn_{13}$ [8], and $Ce_3Ir_4Sn_{13}$ [9]. Itinerant ferromagnetism appears in $Ce_3Os_4Ge_{13}$ [10], and antiferromagnetism in $Nd_3Rh_4Sn_{13}$ [11], $Gd_3Co_4Sn_13$ [12], and $Eu_3Rh_4Sn_{13}$ [13]. Superconductivity with transition temperatures of below 4 K is found in many Remeika compounds; see Table 3 in the topical review article [2]. Superconductivity with a rather high T_c is found in $Yb_3Rh_4Sn_{13}$ (7-8 K) [1] and in compounds with coexisting charge density wave (CDW) and superconductivity in $(Ca,Sr)_3(Rh,Ir)_4Sn_{13}$ series (6 to 8.5 K) [14–17].

In the case of these CDW superconductors, the highest transition temperatures have been found in the vicinity of a quantum critical point (QCP) accessed by pressure [15] and/or by alloying $Sr_3Rh_4Sn_{13}$ (T_{CDW} 135 K) with $Ca_3Rh_4Sn_{13}$ (no CDW) in the $(Ca_xSr_{1-x})_3Rh_4Sn_{13}$ series at around $x = 0.9$ [14, 18]. CDW order is suppressed in $Ca_3Rh_4Sn_{13}$, and the superconducting T_c reaches 8.3 K [19]. Structural QCP was confirmed by X-ray diffraction in the superconducting state, as well as by measurements of the critical current [20–22]. Simultaneously, a non-Fermi-liquid behavior of the electrical resistivity was found, consistent with the presence of QCP.

Alloying $Ca_3Ir_4Sn_{13}$ (T_{CDW} ∼40 K) with $Ca_3Rh_4Sn_{13}$ (no CDW) provides a promising alternative approach to tune the system to a QCP. Here, we report the synthesis and characterization of single crystals of $Ca_3(Ir_{1-x}Rh_x)_4Sn_{13}$.

II. EXPERIMENTAL RESULTS

A. Crystal growth and chemical composition

Single crystals of $Ca_3(Ir_{1-x}Rh_x)_4Sn_{13}$ were grown using a high temperature self-flux method [1, 23, 24]. Pieces of Ca, M and Sn (M = Ir, Rh) were mixed in a 3:4:93 ratio, where M elements were pre-arc melted in the desired stoichiometry for homogenization. The mixture was placed in an alumina crucible, flushed with high-purity argon gas, and vacuum sealed in a quartz tube. The ampule was heated to 1100 °C in a furnace and kept at that temperature for more than 6 hours before cooling to

* Corresponding author:prozorov@ameslab.gov

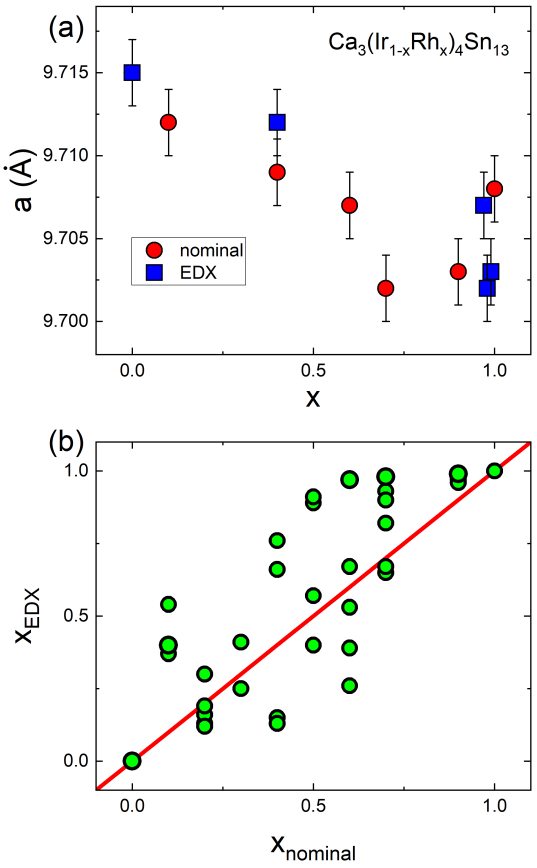

FIG. 1. (a) Cubic lattice parameter a as a function of nominal and EDX-determined composition in $Ca_3(Ir_{1-x}Rh_x)_4Sn_{13}$. (b) Composition determined from EDX, $x_{\rm EDX}$, as function of the nominal composition, $x_{\rm nom}$.

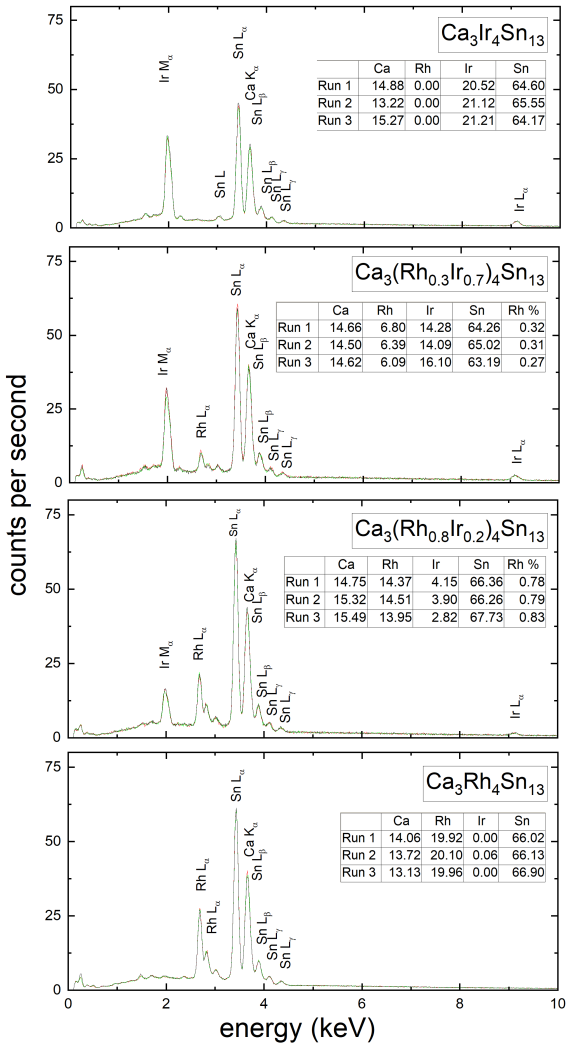

FIG. 2. Energy dispersive X-ray spectra (EDX) used for determination of x in several representative $Ca_3(Ir_{1-x}Rh_x)_4Sn_{13}$ samples, top to bottom x =0.0, 0.31, 0.79, 1.0. Three spectra taken from different locations on the sample surface are plotted, but are not distinguishable due to overlap. The tables show the results of elemental analysis, and % of Rh in intermediate alloy compositions.

800 °C over 30 hours, and 490 °C over 140 hours. Shiny crystals with typical sizes of a few millimeters were obtained after crystal decanting in a centrifuge. The extra residual Sn flux was cleaned by a combination of etching and polishing prior to any measurements. X-ray diffraction (XRD) data were taken with Cu K_α ($\lambda = 0.15418$ nm) radiation from a Rigaku Miniflex powder diffractometer. Figure 1(a) shows the lattice parameter a as a function of the fractional composition of Rh.

B. Sample Selection and Characterization

Due to the high melting temperatures of refractory metals, the Rh / Ir ratio in grown samples showed significant deviations from the loading (nominal) composition. The composition varied both within batches and within individual crystals. The crystals tended to preferentially form $Ca_3Rh_4Sn_{13}$, or compositions very close to it. These crystals exhibited very high purity, but the composition of the entire batch was affected. Figure 1(a) shows the cubic lattice parameter, a, as a function of the nominal composition and the composition determined by EDX. Figure 1(b) shows the correlation between the nominal loading composition and the composition determined by EDX of the resulting crystals. The solid red line shows $x_{\rm EDX} = x_{\rm nom}$ to guide the eye. We can see that there is some trend in the data that follows the expected nominal composition, but the scatter is significant. Because of this, the actual composition of each individual sample was measured using a JEOL scanning electron microscope (SEM) equipped with an Energy Dispersive X-ray spectroscopy (EDX) detector. In each sample, several different spots were examined. For detailed measurements, we selected samples with a relative variation of less than 7%. The superconducting transition of each sample was examined for sharpness and uniformity, which sometimes revealed inhomogeneities within

the bulk of the sample. Each individual curve on every graph in this paper shows a single measurement of a single sample. The samples used for resistivity, magnetization, and penetration depth measurements were not the same samples.

In Fig.2, we show the X-ray spectra used for compositional analysis in EDX measurements. The characteristic lines of individual elements are indicated and their intensity was normalized to obtain the actual composition parameter x. Each frame shows measurements on a single sample, but is plotted with the spectra taken from three separate spots on that sample in different colors. Due to the overlap, only the top run is visible in the figure. These runs are characteristic of the samples selected for the measurements and presented in the paper, and the fitting results are shown in the tables in each panel.

C. Electrical resistivity

Electrical resistivity was measured in single crystals shaped into "resistivity bars" for the four-probe measurements. The size of the as-grown crystals ranged from sub-millimeter to 5 mm. The crystals were etched with HCl, cut with a wire saw, and polished to a typical size of $(1-2)\times 0.2\times 0.4$ mm^3. The contacts were formed by soldering 50 μm silver wires with tin-silver solder [25, 26], with typical contact resistances below 100 $\mu\Omega$.

The resistivity of the samples at $T = 300$ K ranged between 140 and 105 $\mu\Omega\cdot$cm [26]. The precision of the determination of $\rho(300\,\mathrm{K})$ in the alloy samples, which were typically small and irregular in shape, was not sufficient to reveal any systematic dependence on x, so we present the normalized resistivity values, which do not depend on the geometric factor. AC resistivity measurements were performed in a 9 T *Quantum Design* physical property measurement system (PPMS). Although cubic in the normal state, Ir-rich compounds undergo a structural distortion associated with the charge density wave along the $q = (0, 1/2, 1/2)$ ordering vector [14, 27]. This observation is discussed it two alternative models, with the superstructure doubling the unit cell and either leaving the lattice body centered cubic or leading to tetragonal distortion [27]. Although in principle a tetragonal distortion can lead to the appearance of resistivity anisotropy, our measurements in different orientations did not reveal any noticeable difference in the resistivity. This is most likely due to the formation of equivalent tetragonal structural domains, which would average the resistivity anisotropy as it occurs, for example, in $BaFe_2As_2$ [28]. Special means are required to de-twin the samples. Therefore, the measurements presented in this work do not follow any particular orientation.

Figure 3 shows the evolution of the temperature-dependent resistivity (panels a-f) of the $Ca_3(Ir_{1-x}Rh_x)_4Sn_{13}$ single crystals. Panels (g, h, and i) show the derivative of resistivity. To avoid crowding of the data sets, the figure is divided into three groups of panels: (a, d, and g) show Ir-rich compositions showing clear signatures in $\rho(T)$ at the CDW transition; (b, e, and h) show intermediate compositions without clear upturn but still resolvable features in resistivity derivative (see Fig.6 below); (c, f, and i) show Rh-rich compositions. The curves for the samples with the highest x in panels (a) and (b) are repeated with the same color in panels (b) and (c). Similarly, the $x = 0.26$ curve in panel (d) is repeated in panel (e). Panels (d, e, and f) focus on the charge-density wave transition showing the interval from 7 to 44 K, while panels (a), (b) and (c) show the full temperature range. The insets in the upper panels (a, b, and c) focus on the superconducting transitions. The bottom row of the panels (g, h, and i) presents the temperature dependence of the normalized resistivity derivative, $d[\rho(T)/\rho(300K)]/dT$. For iridium-rich compositions (g), the derivative shows a clear minimum with the onset of CDW formation followed by a broad maximum. For $x = 0.51$ curve in panel (h) there is not sufficient data to say that the minimum is above the onset of superconductivity. This suggests that the charge-density wave transition is nearly suppressed. The stars in panels (h) and (i) mark a maximum in the temperature-dependent resistivity derivative. This maximum is first observed on the curve of $x = 0.66$, and it shifts to higher temperatures approaching rhodium end of the compositional range, $x = 1$.

As can be seen from the temperature-dependent resistivity, for all compositions over a broad temperature range, the resistivity reveals a tendency for saturation at high temperatures. A similar type of saturation is found in other charge density wave superconductors, 2H-TaS_2, 2H-$TaSe_2$ and their alloys [29–31]. Similar features are usually discussed in terms of resistivity saturation due to the electronic mean free path becoming comparable to the lattice spacing, in the so-called Mott-Ioffe-Regel limit [32, 33].

D. DC magnetization

DC magnetic susceptibility was measured using a *Quantum Design* vibrating sample magnetometer (VSM) installed in a 9 T PPMS. Figure 4(a) shows magnetic susceptibility extracted from measurements made in warming after the sample was cooled in a zero magnetic field and then a magnetic field of 10 Oe was applied. This is the so-called zero field-cooled (ZFC) measurement protocol. Panel (b) shows the data obtained on cooling from above T_c in a 10 Oe magnetic field. To compare between samples that have different volumes and different shapes (and therefore different demagnetizing factors), the data were normalized by assuming a perfect screening after cooling in a zero field to the base temperature of 2 K. Then, the magnetic susceptibility was evaluated as: $\chi(T) = M(T)/\left|M_{ZFC}(T = 2\,\mathrm{K})\right|$. In this procedure, all ZFC curves start from $\chi(T = 2\,\mathrm{K}) = -1$, but all FC

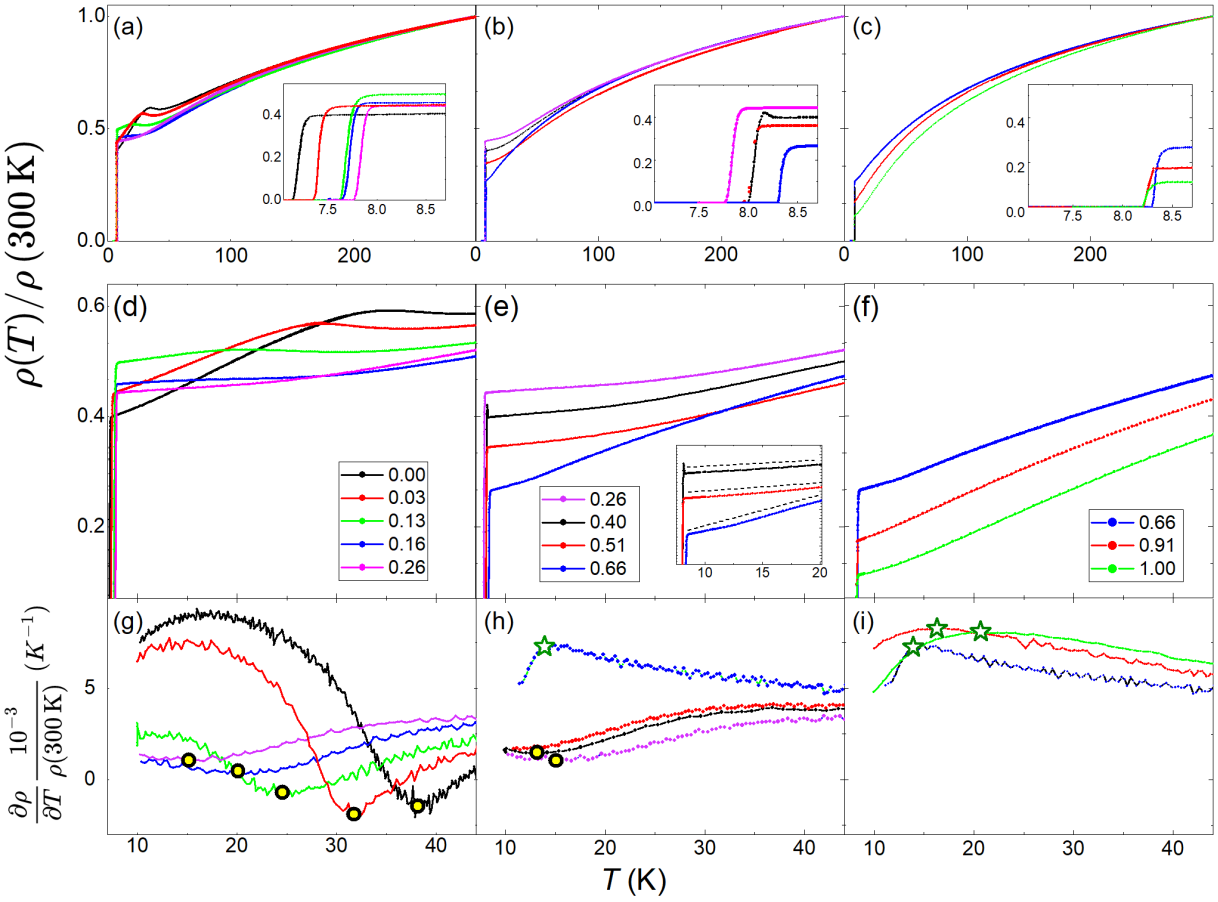

FIG. 3. Temperature-dependent resistivity and its derivative of $Ca_3(Ir_{1-x}Rh_x)_4Sn_{13}$ single crystals normalized by the resistivity value at 300 K. Panels (a, d, and g) show irridium-rich compositions, panels (b, e, and h) show intermediate compositions, and panels (c, f, and i) show rhodium-rich compositions. Panels (a, b, and c) show the full temperature range and the insets zoom in on the superconducting transition. Panels (d, e, and f) zoom in on the temperature range (7 to 44 K) of the charge-density wave transition. As expected, it is clearly visible in panel (d), smeared in panel (e) and absent in panel (f). The inset in panel (e) compares the resistivity just above T_c with the linear temperature dependence shown by the dashed lines drawn to guide the eye. The bottom row of the panels (g, h, and i) shows the evolution of the temperature-dependent normalized resistivity derivative $d[\rho(T)/\rho(300K)]/dT$. The yellow circles in panels (g) and (h) show the position of the derivative minimum, used to define T_{CDW}. The stars in panels (h) and (i) mark a maximum in the derivative, signaling a crossover in the temperature dependence of $\rho(T)$ from close to $T-$linear to a higher power $T-$dependence expected for a Fermi liquid.

curves, shown in Fig.4(b), reflect the actual amount of magnetic flux expelled, which depends on vortex pinning. As shown in Fig.7(c), the flux expulsion upon FC correlates well with the strength of the CDW order, parameterized by $T_{CDW}(x)$, thus implying a direct interaction between the two quantum orders.

E. London penetration depth

The London penetration depth provides further insight into the magnetic properties of $Ca_3(Ir_{1-x}Rh_x)_4Sn_{13}$. Specifically, it allows examination of the genuine Meissner-London state unaffected by Abrikosov vortices and allows for conclusions regarding the superconducting gap structure. Stoichiometric compounds have previously been systematically studied and, although fully gapped, their behavior is unconventional [26, 34]. A full description of the tunnel diode resonator (TDR) technique and its applications can be found elsewhere [35–39]. Briefly, an $LC-$ tank circuit is connected in series with a tunnel diode biased to its regime of negative differential resistance. As a result, an optimized circuit starts resonating spontaneously upon cooling and is always "locked" to its resonant frequency. The temperature of the circuit is actively controlled by a dedicated Lakeshore temperature controller at 5 K with 1 mK accuracy. A superconducting sample on a sapphire rod is inserted into the inductor without touching it, in vacuum, so that its temperature can be changed without disturbing the resonator circuit. Mutual magnetic inductive coupling causes a change in the total magnetic inductance of the circuit and a resonant frequency shift, which is the measured quantity. It can be shown that for each

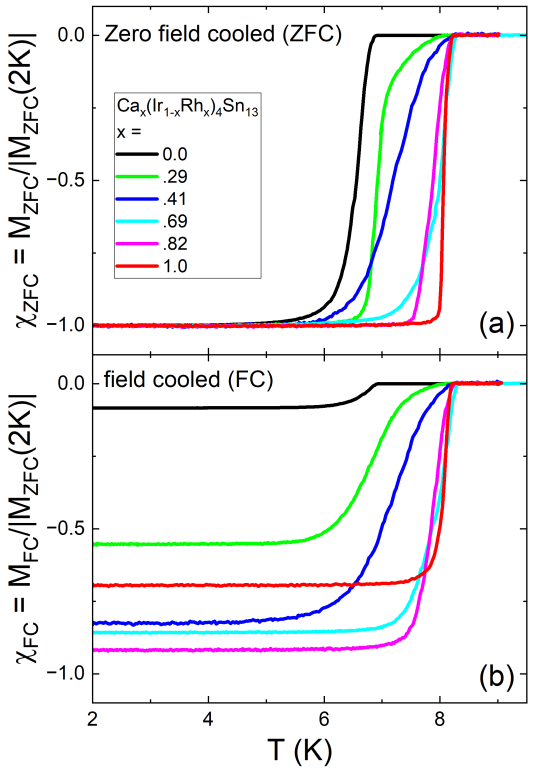

FIG. 4. DC magnetic susceptibility of $Ca_3(Ir_{1-x}Rh_x)_4Sn_{13}$ crystals. (a) After cooling in zero magnetic field, applying a 10 Oe magnetic field and taking the measurements on warming (ZFC); (b) taking measurements on cooling in a magnetic field of 10 Oe. The normalization in both panels is done assuming a perfect screening at $T = 2$ K, see text for details.

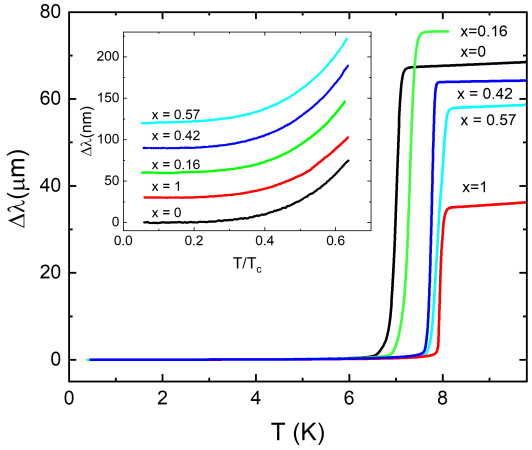

FIG. 5. London penetration depth in $Ca_3(Ir_{1-x}Rh_x)_4Sn_{13}$ single crystals of the indicated Rh compositions. The main panel shows the full temperature range of transitions. The saturation just above the transition occurs when penetration depth starts to diverge and becomes of the order of the sample size. Due to different sample sizes, there is no systematic behavior here. The inset zooms at the low-temperature region, this time plotted as function of the reduced temperature, T/T_c. The curves are shifted vertically by a constant for visual clarity. Roughly below $T < 0.35T_c$, all curves saturate indicating exponential attenuation, hence a fully gapped state, at all x.

sample, the frequency change, $\Delta f = -G\chi$, where Δf is measured with respect to the value without the sample (empty coil). Details of the calibration procedure and the calibration constant G are described elsewhere [38, 39]. The magnetic susceptibility in a Meissner-London state (no Abrikosov vortices) of a superconductor of any shape can be described by $\chi = \lambda/R \tanh(R/\lambda) - 1$, where λ is the London penetration depth and R is the so-called effective dimension, which is a function of the real sample dimensions [38, 39]. For typical samples in this research, $R \sim 100 - 200$ μm. Therefore, for most of the temperature interval, we can set $\tanh R/\lambda \approx 1$ and, therefore, $\delta f(T) \sim \Delta\lambda(T)$, where δf is counted from the state at the base temperature, because we are only interested in the low-temperature variation of $\lambda(T)$. The circuit stability is such that we resolve the changes in frequency of the order of 0.01 Hz, which based on the main frequency of 14 MHz means that we have a resolution of 1 part per billion. For our crystals, this translates to sub-angstrom level sensitivity.

Figure 5 shows the London penetration depth in $Ca_3(Ir_{1-x}Rh_x)_4Sn_{13}$ crystals with indicated Rh content. The main panel shows the full temperature range with sharp transitions to the normal state. The saturation just above the transitions occurs when the penetration depth starts to diverge approaching T_c and becomes comparable to the sample size. As described above, in this case, $\lim_{x\to\infty}[\chi = x\tanh(1/x) - 1] \to 0$ and the measurable signal becomes insensitive to further changes. Comparing with Fig.4(a) we find similar-looking curves, because they both depict measurements of $\chi(T)$. We note that complete shielding of the small excitation field, apparent in Fig.5, justifies the normalization of the DC magnetic susceptibility measured in 10 Oe after zero-field cooling, Fig.4(a). However, if we zoomed in Fig.4(a) to low temperatures, we would only find noise, because commercial susceptometers are only sensitive at about 1 part per million. In the case of TDR, with a three orders of magnitude better sensitivity, we can study the structure of $\lambda(T)$, which is directly related to the superconducting order parameter [38]. The inset in Figure 5 zooms in on the low-temperature region, this time plotted as a function of the reduced temperature, T/T_c. The curves are shifted vertically by a constant for the sake of clarity. Approximately below $T < 0.35T_c$, all curves saturate, indicating exponential attenuation and, therefore, a fully gapped state at all x. Previously, we reported exponential attenuation in pure compounds $x = 0$ and $x = 1$, indicating a fully gaped Fermi surface [26]. However, probing the robustness of the superconducting state to disorder, we found a significant reduction of the transition temperature with non-magnetic scattering and it was concluded that 3-4-13 stannides are indeed fully gapped, but their order parameter is unconventional [26]. It seems that this trend persists uniformly in the Ir/Rh alloys, open-

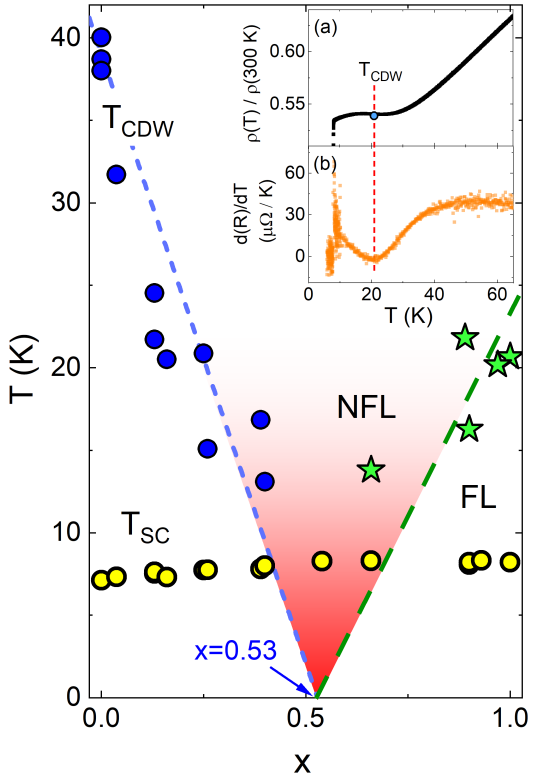

FIG. 6. Summary phase diagram of $Ca_3(Ir_{1-x}Rh_x)_4Sn_{13}$ alloy. Blue dots show the CDW transition temperature, $T_{CDW}(x)$, determined from the position of the minimum in the temperature-dependent derivative of resistivity shown in the panels (g) and (h) of Fig.3. The blue short-dashed line in the main panel shows a linear fit with a fixed intercept (39 K from the well-defined transition temperature for the x=0 samples), best fit gives $T_{CDW}(x) \approx 39.0-73.8x$, which extrapolates to zero at $x \approx 0.53$. The inset (a) shows an example of normalized resistivity vs. temperature (at $x = 0.22$) exhibiting a pronounced upturn upon cooling due to the opening of the CDW gap on part of the Fermi surface. Insets (a) and (b) show the correspondence between the temperature dependence of resistivity (a) and the resistivity derivative $d[\rho/\rho(300K)]/dT$ (b), with the dashed line showing the position of the minimum used to determine T_{CDW}. Green stars show the temperature at which the derivative of the resistivity is at a maximum (see the green stars in panels (h) and (i) in Fig.3), and is used to separate the high-temperature resistivity and low-temperature possible Fermi liquid T^2- regimes for compositions $x >0.53$. The green dashed line in the main panel is guide for eyes through green stars showing the expected vanishing of the Fermi-liquid behavior at QCP. The yellow circles in the main panel show the composition evolution of the superconducting transition temperature.

ing up possibilities for studying various effects, such as non-exponential attenuation of the London penetration depth in the vicinity of the QCP [40].

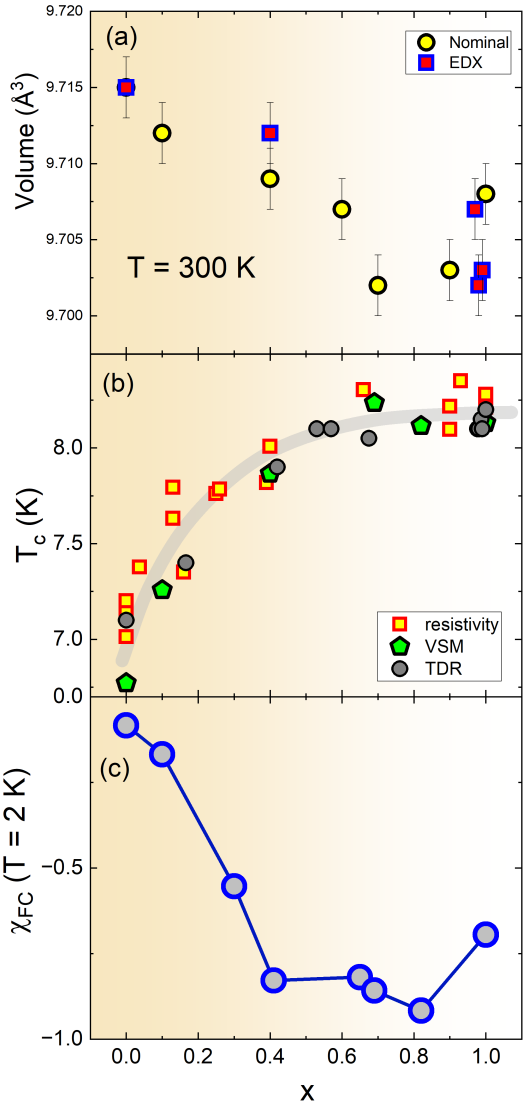

FIG. 7. Composition dependence of: (a) the unit cell volume at $T = 300\,K$; (b) the superconducting transition temperature, T_c, obtained from electrical resistivity measurements (red-yellow squares), DC magnetization measurements using VSM magnetometer (black-green pentagons) and tunnel-diode resonator (TDR) London penetration depth measurements (grey dots). The wide light grey line is guide to eyes to show a general trend. Panel (c) shows composition evolution of the magnetic susceptibility in field cooled protocol $\chi_{FC}(T = 2\,K)$, revealing strong suppression of the Meissner expulsion in the CDW composition.

III. ANALYSIS AND DISCUSSION

We now summarize and review the results, focusing on trends in the entire range of compositions, from pure Ir ($x = 0$) to pure Rh ($x = 1$). In Fig.6, we present the summary phase diagram of the novel alloy $Ca_3(Ir_{1-x}Rh_x)_4Sn_{13}$. To illustrate the definition of T_{CDW}, the inset (a) shows a normalized resistivity vs. temperature curve ($x = 0.22$) with a clear upturn on cool-

ing, expected due to the opening of the partial gap on the Fermi surface by the CDW $T_{\rm CDW}$. The inset (b) shows the temperature derivative of this curve with a minimum at the CDW transition. Nuclear magnetic resonance (NMR) Knight shift measurements directly confirmed that CDW formation reduces the density of states at the Fermi surface by approximately 10% of the total DOS in the $x = 0$ composition [41]. The blue circles in Fig.6 show $T_{\rm CDW}(x_{\rm EDX})$ determined using this criterion. The dashed blue line shows a linear fit with the $y-$axis intercept fixed at 39.0 K, resulting in $T_{\rm CDW}(x) \approx 39.0-73.8x$. This value of $T_{\rm CDW}(x = 0) = 39.0\,{\rm K}$ is the literature average of known data in well-studied stoichiometric $Ca_3Ir_4Sn_{13}$ crystals. This line extrapolates to zero at $x \approx 0.53$. With the intercept on the $y-$ axis as a free parameter, the linear fit yields $T_{\rm CDW}(x) \approx 35.2 - 60.7x$, which extrapolates to $x \approx 0.58$. Therefore, if the line of the CDW transition continues linearly below the superconducting dome, the putative QCP should be located somewhere between $x \approx 0.53$ and $x \approx 0.58$. We note that resistivity values in the immediate vicinity above T_c decrease significantly outside the CDW composition range, as expected due to the closure of the CDW gap on the Fermi surface.

It is expected that in the vicinity of a QCP, the resistivity temperature dependence deviates strongly from the conventional T^2 Fermi liquid behavior towards $T-$linear variation [42, 43]. This was demonstrated in pressure-tuned $Ca_3Ir_4Sn_{13}$ [14] and in the study of a combination of Ca-Sr alloying and pressure [15]. Inspecting our resistivity curves around the expected QCP compositions in Fig.3(e) indeed finds close to a $T-$linear behavior, particularly in the sample with $x = 0.51$. To highlight this, we show a dashed line in the inset. Away from the QCP composition, theoretically, it is expected that the temperature dependence of the resistivity changes from the Fermi liquid T^2 behavior to $T-$linear upon warming. The $T-$derivative of resistivity is then expected to change from $T-$ linear to a constant. Panels (h) and (i) of Fig.3 demonstrate a clear change from fast to slow variation of the resistivity derivative with temperature. The green stars mark the temperature of the crossover, which we interpret as a crossover from Fermi liquid (FL) to non-Fermi liquid (NFL) behavior. The green stars in Fig.6 mark this crossover. A guide to an eye dashed line extrapolates to the same range of QCP concentrations, thus forming the so-called "QCP funnel".

A general expectation in a QCP scenario is that the transition temperature T_c reaches a maximum at the QCP if quantum fluctuations serve as a pairing glue [42]. Yellow circles in Fig.6 show the superconducting transition temperature determined from the resistivity. On this scale, it appears practically independent of x. A more detailed behavior is shown in Fig.7, which presents the results of three independent measurements. Electrical resistivity (red-yellow squares), DC magnetization (green pentagons), and TDR London penetration depth measurements (gray circles) all reveal a rising curve that flattens at $x \gtrsim 0.6$. A $T_c(x)$ increase towards $x \sim 0.5$ reflects the competition between CDW and superconductivity, although the absolute variation in T_c is not large, from 7 K to 8.3 K. The observation of a plateau in $T_c(x)$ dependence rather than of a "dome shape" is different from the behavior of high$-T_c$ cuprates [43], heavy fermions [42] and in phosphorus doped 122 iron-based superconductors [44]. It may suggest that the competition between CDW and superconductivity for the states at Fermi energy, leading to a decrease of T_c, is stronger than the effect of quantum fluctuations. Synchrotron X-ray and Raman spectroscopy studies under pressure of $Ca_3Rh_4Sn_{13}$ and related Sr and La compounds revealed the volume of the unit cell as a parameter controlling the phase diagram [45], similar to closely related 5-6-18 compounds [46]. The top panel of Fig.7 shows the composition evolution of the unit cell volume in $Ca_3(Ir_{1-x}Rh_x)_4Sn_{13}$. Although the volume clearly decreases for x <0.5, it becomes nearly constant within error bars for higher x. Perhaps there is a correlation with the compositional dependence of $T_c(x)$.

Another important observation of the compositional evolution of properties is found in the amount of Meissner expulsion of a weak magnetic field. Fig.7(c) shows magnetic susceptibility values at $T = 2\,{\rm K}$ after cooling in a 10 Oe magnetic field as a function of Rh composition, x. Remarkably, there is a clear correlation with the region of the charge density wave. The degree of flux expulsion is progressively smaller where CDW is stronger, judging by the CDW transition temperature (see Fig.6). This points to weakened superconductivity in the CDW domain, which implies a direct link between the CDW (and/or structural distortion) and the superconducting condensation energy. Therefore, we can expect a significant effect if the CDW transition line $T_{\rm CDW}\,(x)$ terminates at $T = 0$ as a second-order quantum phase transition resulting in a QCP (as in the related systems $(Sr_{1-x}Ca_x)_3Ir_4Sn_{13}$ [14, 15, 47] and $(Sr_{1-x}Ca_x)_3Rh_4Sn_{13}$ [15, 47].)

IV. CONCLUSIONS

In conclusion, we report physical and structural characterization of the novel members of the Remeika quasiskutterudites $Ca_3(Ir_{1-x}Rh_x)_4Sn_{13}$ single crystals at ambient pressure. The superconducting transition temperature increases from 7 K ($x = 0$) to 8.3 K ($x = 1$). The charge density wave (CDW) transition is suppressed with increasing x, extrapolating linearly to $x_c \approx 0.53 - 0.58$ under the superconductivity dome. Magnetization and transport measurements show a significant influence of CDW on the superconducting phase. In particular, Meissner expulsion is suppressed in the CDW region, and the normal state resistivity above T_c is significantly larger in this part of the phase diagram. The superconducting T_c does not peak around x_c but rather saturates at $x > x_c$. The London penetration depth is attenu-

ated exponentially upon cooling for all compositions, indicating a fully gapped superconducting state. Overall, $Ca_3(Ir_{1-x}Rh_x)_4Sn_{13}$ appears to be a suitable system for finding a QCP at ambient pressure. Supporting this idea is the observation of a close to $T-$linear temperature-dependent resistivity for $x > x_c$ and a gradual decrease in the temperature of non-Fermi-liquid to Fermi liquid crossover on approaching QCP from the high x side.

ACKNOWLEDGMENTS

This work was supported by the National Science Foundation under Grant No. DMR-2219901. M. A. T. and K. R. J. were supported by the U.S. Department of Energy (DOE), Office of Science, Basic Energy Sciences, Materials Science and Engineering Division. Ames National Laboratory is operated for the U.S. DOE by Iowa State University under Contract No. DE-AC02-07CH11358. C. P. acknowledges support by the U.S. Department of Energy, Basic Energy Sciences, Division of Materials Science and Engineering, under Contract No. DE-SC0012704 (BNL).

[1]J. P. Remeika, G. P. Espinosa, A. S. Cooper, H. Barz, J. M. Rowell, D. B. McWhan, J. M. Vandenberg, D. E. Moncton, Z. Fisk, L. D. Woolf, H. C. Hamaker, M. B. Maple, G. Shirane, and W. Thomlinson, A new family of ternary intermetallic superconducting/magnetic stannides, Solid State Comm. **34**, 923 (1980).

[2]R. Gumeniuk, Chapter 304 - structural and physical properties of remeika phases, in *Including Actinides*, Handbook on the Physics and Chemistry of Rare Earths, Vol. 54, edited by J.-C. G. Bünzli and V. K. Pecharsky (Elsevier, 2018) pp. 43–143.

[3]R. K. Kamadurai, M. O. Ogunbunmi, H. S. Nair, and A. M. Strydom, Semiconducting behaviour in the remeika phase: $Pr_3Ir_4Ge_{13}$, Journal of Alloys and Compounds **872**, 159481 (2021).

[4]R. Gumeniuk, K. O. Kvashnina, W. Schnelle, A. Leithe-Jasper, and Y. Grin, Magnetic and transport properties of structural variants of remeika phases: $th_3ir_4ge_{13}$ and $u_3ir_4ge_{13}$, Phys. Rev. B **91**, 094110 (2015).

[5]H. Kong, X. Shi, C. Uher, and D. Morelli, Thermoelectric properties of rare earth-rutheniumgermanium compounds, Journal of Applied Physics **102**, 10.1063/1.2753592 (2007), cited by: 10.

[6]E. L. Thomas, H.-O. Lee, A. N. Bankston, S. MaQuilon, P. Klavins, M. Moldovan, D. P. Young, Z. Fisk, and J. Y. Chan, Crystal growth, transport, and magnetic properties of $Ln_3Co_4Sn_{13}$ (Ln=La, Ce) with a perovskite-like structure, J. Solid State Chem. **179**, 1642 (2006).

[7]M. O. Ogunbunmi and A. M. Strydom, Promising thermoelectric properties of heavy-fermion semimetal $Pr_3Os_4Ge_{13}$, J. Phys. Condens. Mat. **32**, 405606 (2020).

[8]U. Köhler, A. P. Pikul, N. Oeschler, T. Westerkamp, A. M. Strydom, and F. Steglich, Low-temperature study of the strongly correlated compound $Ce_3Rh_4Sn_{13}$, Journal of physics. Condensed matter **19**, 386207 (2007).

[9]H. Sato, T. Fukuhara, S. Iwakawa, Y. Aoki, I. Sakamoto, S. Takayanagi, and N. Wada, Magnetic and transport properties of $Re_3Ir_4Sn_{13}$, Physica B: Condensed Matter **186-188**, 630 (1993).

[10]O. Prakash, A. Thamizhavel, and S. Ramakrishnan, Ferromagnetic ordering of minority Ce^{3+} spins in a quasi-skutterudite $Ce_3Os_4Ge_{13}$ single crystal, Phys. Rev. B **93**, 064427 (2016).

[11]S. Sahu and A. Hallas, Antiferromagnetism and field-induced transitions in single crystals of the Remeika phase compound $Nd_3Rh_4Ge_{13}$, in *APS March Meeting Abstracts*, APS Meeting Abstracts, Vol. 2023 (2023) p. T56.009.

[12]M. A. Pires, L. M. Ferreira, J. G. S. Duque, R. R. Urbano, O. Agüero, I. Torriani, C. Rettori, E. M. Bittar, and P. G. Pagliuso, Crystal structure and physical properties of $Gd_3Co_4Sn_{13}$ intermetallic antiferromagnet, Journal of Applied Physics **99**, 08J311 (2006).

[13]P. Bordet, J. Hodeau, P. Wolfers, S. Miraglia, A. Benoit, M. Marezio, and J. Remeika, Magnetic structures of $SnEu_3Rh_4Sn_{12}$ and $(Sn_{0.58}Er_{0.42})Er_4Rh_6Sn_{18}$, Physica B+C **136**, 432 (1986), neutron Scattering.

[14]L. E. Klintberg, S. K. Goh, P. L. Alireza, P. J. Saines, D. A. Tompsett, P. W. Logg, J. Yang, B. Chen, K. Yoshimura, and F. M. Grosche, Pressure and composition induced structural quantum phase transition in the cubic superconductor $(Sr,Ca)_3Ir_4Sn_{13}$, Phys. Rev. Lett. **109**, 237008 (2012).

[15]S. K. Goh, D. A. Tompsett, P. J. Saines, H. C. Chang, T. Matsumoto, M. Imai, K. Yoshimura, and F. M. Grosche, Ambient pressure structural quantum critical point in the phase diagram of $(Ca_xSr_{1-x})_3Rh_4Sn_{13}$, Phys. Rev. Lett. **114**, 097002 (2015).

[16]A. F. Fang, X. B. Wang, P. Zheng, and N. L. Wang, Unconventional charge-density wave in $sr_3ir_4sn_{13}$ cubic superconductor revealed by optical spectroscopy study, Phys. Rev. B **90**, 035115 (2014).

[17]H.-T. Wang, M. K. Srivastava, C.-C. Wu, S.-H. Hsieh, Y.-F. Wang, Y.-C. Shao, Y.-H. Liang, C.-H. Du, J.-W. Chiou, C.-M. Cheng, J.-L. Chen, C.-W. Pao, J.-F. Lee, C. N. Kuo, C. S. Lue, M.-K. Wu, and W.-F. Pong, Electronic and atomic structures of the sr3ir4sn13 single crystal: A possible charge density wave material, Scientific reports **7**, 40886 (2017).

[18]Y. W. Cheung, Y. J. Hu, M. Imai, Y. Tanioku, H. Kanagawa, J. Murakawa, K. Moriyama, W. Zhang, K. T. Lai, K. Yoshimura, F. M. Grosche, K. Kaneko, S. Tsutsui, and S. K. Goh, Evidence of a structural quantum critical point in $(Ca_xSr_{1-x})_3Rh_4Sn_{13}$ from a lattice dynamics study, Phys. Rev. B **98**, 161103R (2018).

[19]J. P. A. Westerveld, D. M. R. L. Cascio, and H. Bakker, Arrhenius behaviour of the degradation of the transition temperature in the ternary superconductors $Yb_3Rh_4Sn_{13}$ and $Ca_3Rh_4Sn_{13}$, J. Phys. F: Metal Physics **17**, 1963 (1987).

[20]L. S. I. Veiga, J. R. L. Mardegan, M. v. Zimmermann, D. T. Maimone, F. B. Carneiro, M. B. Fontes, J. Strempfer, E. Granado, P. G. Pagliuso, and E. M. Bittar, Possible quantum fluctuations in the vicinity of the quantum critical point of $(Sr,Ca)_3Ir_4Sn_{13}$revealed by high-energy x-ray diffraction, Phys. Rev. B **101**, 104511 (2020).

[21]P. Upreti, M. Krogstad, C. Haley, M. Anitescu, V. Rao, L. Poudel, O. Chmaissem, S. Rosenkranz, and R. Osborn, Order-disorder transitions in $(Ca_xSr_{1-x})_3Rh_4Sn_{13}$, Phys. Rev. Lett. **128**, 095701 (2022).

[22]X. Liu, W. Zhang, K. T. Lai, K. Moriyama, J. L. Tallon, K. Yoshimura, and S. K. Goh, Peak in the critical current density in $(Ca_xSr_{1-x})_3Rh_4Sn_{13}$ tuned towards the structural quantum critical point, Phys. Rev. B **105**, 214524 (2022).

[23]G. Espinosa, Crystal growth and crystal-chemical investigation of systems containing new superconducting and/or magnetic ternary stannides, Mater. Res. Bull. **15**, 791 (1980).

[24]K. Wang and C. Petrovic, Ca $_3Ir_4Sn_{13}$: A weakly correlated nodeless superconductor, Phys. Rev. B **86**, 024522 (2012).

[25]M. A. Tanatar, N. Ni, S. L. Bud'ko, P. C. Canfield, and R. Prozorov, Field-dependent transport critical current in single crystals of $Ba(Fe_{1-x}TM_x)_2As_2$ (TM = Co, Ni) superconductors, Supercond. Sci. Technol. **23**, 054002 (2010).

[26]E. H. Krenkel, M. A. Tanatar, M. Kończykowski, R. Grasset, E. I. Timmons, S. Ghimire, K. R. Joshi, Y. Lee, L. Ke, S. Chen, C. Petrovic, P. P. Orth, M. S. Scheurer, and R. Prozorov, Possible unconventional pairing in $(Ca,Sr)_3(Ir,Rh)_4Sn_{13}$ superconductors revealed by controlling disorder, Phys. Rev. B **105**, 094521 (2022).

[27]D. G. Mazzone, S. Gerber, J. L. Gavilano, R. Sibille, M. Medarde, B. Delley, M. Ramakrishnan, M. Neugebauer, L. P. Regnault, D. Chernyshov, A. Piovano, T. M. Fernández-Díaz, L. Keller, A. Cervellino, E. Pomjakushina, K. Conder, and M. Kenzelmann, Crystal structure and phonon softening in $Ca_3Ir_4Sn_{13}$, Phys. Rev. B **92**, 024101 (2015).

[28]M. A. Tanatar, E. C. Blomberg, A. Kreyssig, M. G. Kim, N. Ni, A. Thaler, S. L. Bud'ko, P. C. Canfield, A. I. Goldman, I. I. Mazin, and R. Prozorov, Uniaxial-strain mechanical detwinning of $CaFe_2As_2$ and $BaFe_2As_2$ crystals: Optical and transport study, Phys. Rev. B **81**, 184508 (2010).

[29]M. Naito and S. Tanaka, Electrical transport properties in 2H-NbS_2, -$NbSe_2$, -TaS2 and -$TaSe_2$, J. Phys. Soc. Jpn. **51**, 219 (1982).

[30]M. Naito and S. Tanaka, Galvanomagnetic effects in the charge-density-wave state of 2H-$NbSe_2$ and 2H-$TaSe_2$, J. Phys. Soc. Jpn. **51**, 228 (1982).

[31]L. Li, X. Deng, Z. Wang, Y. Liu, M. Abeykoon, E. Dooryhee, A. Tomic, Y. Huang, J. B. Warren, E. S. Bozin, S. J. L. Billinge, Y. Sun, Y. Zhu, G. Kotliar, and C. Petrovic, Superconducting order from disorder in 2H-$TaSe_{2-x}S_x$, npj Quantum Materials **2**, 11 (2017).

[32]P. B. Allen, Metals with small electron mean-free path: saturation versus escalation of resistivity, Physica B **318**, 24 (2002).

[33]O. Gunnarsson, M. Calandra, and J. E. Han, Colloquium: Saturation of electrical resistivity, Rev. Mod. Phys. **75**, 1085 (2003).

[34]J. Luo, J. Yang, S. Maeda, Z. Li, and G.-Q. Zheng, Structural phase transition, precursory electronic anomaly, and strong-coupling superconductivity in quasiskutterudite $(Sr_{1-x}Ca_x)_3Ir_4Sn_{13}$ and $Ca_3Rh_4Sn_{13}$, Chinese Physics B **27**, 077401 (2018).

[35]C. T. Van Degrift, Tunnel diode oscillator for 0.001 ppm measurements at low temperatures, Rev. Sci. Instrum. **46**, 599 (1975).

[36]R. Prozorov, R. W. Giannetta, A. Carrington, and F. M. Araujo-Moreira, Meissner-London state in superconductors of rectangular cross section in a perpendicular magnetic field, Phys. Rev. B **62**, 115 (2000).

[37]R. Prozorov, R. W. Giannetta, A. Carrington, P. Fournier, R. L. Greene, P. Guptasarma, D. G. Hinks, and A. R. Banks, Measurements of the absolute value of the penetration depth in high-T-c superconductors using a low-T-c superconductive coating, Appl. Phys. Lett. **77**, 4202 (2000).

[38]R. Prozorov and R. W. Giannetta, Magnetic penetration depth in unconventional superconductors, Supercond. Sci. Technol. **19**, R41 (2006).

[39]R. Prozorov, Meissner-London susceptibility of superconducting right circular cylinders in an axial magnetic field, Phys. Rev. App. **16**, 024014 (2021).

[40]J. Hasan, M. Dzero, M. Khodas, and A. Levchenko, Thermodynamic properties of nodal superconductors close to a magnetic quantum critical point, Phys. Rev. B **105**, 054510 (2022).

[41]B. Chen, J. Yang, Y. Guo, and K. Yoshimura, 119sn NMR study in the normal state of the superconductor $Ca_3Ir_4Sn_{13}$, Europhysics Letters **111**, 17005 (2015).

[42]N. D. Mathur, F. M. Grosche, S. R. Julian, I. R. Walker, D. M. Freye, R. K. W. Haselwimmer, and G. G. Lonzarich, Magnetically mediated superconductivity in heavy fermion compounds, Nature **394**, 39 (1998).

[43]L. Taillefer, Scattering and pairing in cuprate superconductors, Ann. Rev. Cond. Matt. Phys. **1**, 51 (2010).

[44]Y. Nakai, T. Iye, S. Kitagawa, K. Ishida, H. Ikeda, S. Kasahara, H. Shishido, T. Shibauchi, Y. Matsuda, and T. Terashima, Unconventional superconductivity and antiferromagnetic quantum critical behavior in the isovalent-doped $BaFe_2(As,P)_2$, Phys. Rev. Lett. **105**, 107003 (2010).

[45]M. Sundaramoorthy, B. Joseph, G. Lingannan, P. Kumar Mondal, C. Nung Kuo, C. Shan Lue, and S. Arumugam, Pressure effects on superconducting quasiskutterudite $Sr_3Rh_4Sn_{13}$ compared to the ambient pressure properties of $Ca_4Rh_4Sn_{13}$ and $La_3Rh_4Sn_{13}$ compounds, Physica Status Solidi (RRL) **17**, 2300078 (2023).

[46]M. Sundaramoorthy, B. Joseph, G. Lingannan, P. K. Mondal, R. Sokkalingam, C. Lue, C. Kuo, and S. Arumugam, Structural and vibrational properties of cage-type $Sc_5Ru_6Sn_{18}$ superconductor under pressure using synchrotron x-ray diffraction and raman spectroscopy, Journal of Alloys and Compounds **973**, 172905 (2024).

[47]Y. W. Cheung, Y. J. Hu, M. Imai, Y. Tanioku, H. Kanagawa, J. Murakawa, K. Moriyama, W. Zhang, K. T. Lai, K. Yoshimura, F. M. Grosche, K. Kaneko, S. Tsutsui, and S. K. Goh, Evidence of a structural quantum critical point in $(Ca_xSr_{1-x})_3Rh_4Sn_{13}$ from a lattice dynamics study, Phys. Rev. B **98**, 161103 (2018).